Water and Soil Management and Modeling

Online ISSN: 2783 - 2546

University of Mohaghegh Ardabili

Simulating and investigating the impact of bedform geometric features on flow structure in three-dimensional dunes

Masoumeh Ghodousi [1], Elham Fazel Najafabadi [2]*

[1] Former M.Sc. Student, Department of Water Sciences and Engineering, College of Agriculture, Isfahan University of Technology, Isfahan, Iran
[2] Assistant Professor, Department of Water Sciences and Engineering. College of Agriculture, Isfahan University of Technology, Isfahan, Iran

Abstract

The river bed forms are noteworthy from the hydraulic and environmental point of view. For many years, river engineers have researched the flow structure in the presence of sandy river bedforms. Due to the limitations in laboratory and field studies, numerical methods can accurately examine the flow structure of river bedforms. In this research, flow simulation on three-dimensional dunes was performed using computational fluid dynamics (CFD). Also, the effect of changes in bed form angle, bed form wavelength, and the curvature of the three-dimensional dune crest line was investigated. The results showed that in the lobe-shaped dune at the centerline channel, the maximum stream-wise velocity was 20cm/s; however, for the saddle-shaped dune, a similar value was 31cm/s. Also, the separation zone is 7cm and 30cm for the lobe- and saddle-shaped bedforms, respectively. Also, increasing the lee-side angle from 15 to 30 degrees caused the 20% velocity reduction at the dune crest, for the lobe- and saddle-shaped bedform; however, 50% and 10% reduction in the stream-wise velocity was illustrated at the lee-side, for the lobe- and saddle-shaped bedform, respectively. Meanwhile, for the saddle-shaped bedform, the velocity increased and the Reynolds shear stress decreased with the decrease of the exit angle. Increasing the wavelength from 25 to 96 cm showed the 20% stream-wise velocity reduction at the dune crest, for the lobe- and saddle-shaped bedform; however, 40% and 10% reduction in the stream-wise velocity was illustrated at the lee-side, for the lobe- and saddle-shaped bedform, respectively. Decreasing the curvature crest line showed a 15% reduction and 20% increase in stream-wise velocity at the dune crest, for the lobe- and saddle-shaped bedform, respectively; however, a 50% reduction and 20% increase in the stream-wise velocity was illustrated at the lee-side, for the lobe- and saddle-shaped respectively. Meanwhile, for the saddle-shaped bedform, the increase in the curvature of the crest line has led to a decrease in velocity and, in most cases, an increase in Reynolds shear stress.

Keywords: Simulation, OpenFoam, Velocity, Shear stress, three-dimensional dune.

Article Type: Research Article
Academic Editor: Raoof Mostafazadeh

*Corresponding Author, E-mail: efazel@iut.ac.ir
Citation: Ghodousi, M., & Fazel Najafabadi, E. (2026). Simulating and investigating the impact of bedform geometric features on flow structure in three-dimensional dune. Water and Soil Management Modeling, 6 (Special Issue: New Approaches to Water and Soil Management and Modeling), 67-88.
doi: 10.22098/mmws.2025.18557.1705
Received: 16 October 2025, Received in revised form: 07 November 2025, Accepted: 07 November 2025, Published online: 03 June 2026
Water and Soil Management and Modeling, Year 2026, Vol. 6, Special Issue, pp. 67-88
Publisher: University of Mohaghegh Ardabili

1. Introduction

Rivers are vital for their surrounding regions, serving as essential water sources for human populations. Most rivers and alluvial channels have uneven bed surfaces caused by sediment movement (Raudkivi 1963, Hassanzadeh et al. 2024, Roushangar et al. 2024). This movement results in structures known as bed-forms. These bed forms develop from the interaction between water flow and the materials on the riverbed. Recent scientific studies have placed greater emphasis on "bed forms," exploring the complex relationships among turbulent flow dynamics, sediment transport, and the evolution of bed forms (Maddux et al. 2003; Mazumder et al. 2009; Motamedi et al. 2012, 2014). Pool-riffle bed forms are formed in sandy rivers (MacVicar and Rennie 2012), and dune bed forms are formed in sandy rivers and beds. Dunes in rivers are categorized into two forms: two-dimensional dunes for low flow velocities and three-dimensional dunes for high velocities with similar particle sizes (Balachandar and Patel 2008, Parsons et al. 2005). Typically, sand waves assume a triangular, asymmetrical cross-sectional shape with specific angles on the lee-side and stoss-side, generating vortex flow and a flow separation zone that dissipates energy (Stoesser et al. 2008).

Turbulent flow parameters, such as Reynolds stresses, play a key role in influencing sediment transport, which in turn shapes and evolves bed-forms. Concurrently, the morphology of the bed impacts flow characteristics by affecting resistance forces, roughness changes, and occasional flow separations. The presence of bed-forms influences the velocity profile near the bed surface, altering flow resistance and the transfer rates of bed-and suspended-load. Research by Grant and Madsen (1982), as well as Van Rijn (1993), has underscored the critical importance of these factors. Observations of velocities within the separation zone show a decrease compared to the average flow velocity in the stoss-side (upstream slope of the dune). Early studies by Raudkiwi (1963), despite using less advanced methodologies, remain significant for their contributions to understanding dune behavior.

The term "dune" was originally introduced by Gilbert (1914), with the classification of dunes presented by Ashley (1990). Hence, special attention has been paid to studying turbulence flow structure on a fixed bed in the laboratory (Spalart and Allmaras 1992). Many researchers have worked on 2D dunes experimentally, numerically, and in the field, such as Cisneros and Best (2024); Ma et al (2024); Sharifi et al. (2023), Mazumder et al. (2009); Stoesser et al. (2008); Ojha and Mazumder (2008). However, fewer studies have investigated the flow structure in the presence of three-dimensional dunes.

Subsequent studies by researchers such as Maddox et al. (2003), Venditti (2003), Best (2005), and Parsons et al. (2005) have delved further into the complexities of three-dimensional dunes and their influence on flow dynamics. These studies have highlighted the unique effects of varying dune bedforms on flow patterns and vortices, emphasizing the need for comprehensive field studies to complement laboratory investigations. Maddox et al. (2003) studied three-dimensional dunes that had a straight crest line, but the height of the dune changed in the lateral direction of the flow in the form of a cosine wave. These researchers found that this method of change, in comparison with the flow in three-dimensional dunes with the same crest height, significantly changes the components of the flow. The maximum velocity is in the direction of the flow on the crest line, and a significant amount of the momentum flux above the dune is generated through secondary currents and transferred by the topography resulting from the three-dimensionality of the dune. Parsons et al. (2005) stated that the three-dimensionality of the dune has a significant effect on the flow structure, and both bedform patterns with convex and concave crest lines towards the downstream side create smaller areas of flow separation on the downstream side of the bedform.

In short, the findings from these studies emphasize the significant impact of three-dimensional dune bedforms on flow patterns, suggesting implications for sediment transport processes and river morphology. The interdisciplinary nature of research into riverbed dynamics underscores the challenges in accurately capturing and analyzing the turbulent structures caused by natural bed-forms in river environments (Maddux et al. 2003; Venditti 2003; Best 2005; Parsons et al. 2005).

Omidyeganeh and Piomelli (2013) performed large-eddy simulations of the flow over a series of three-dimensional (3D) dunes at laboratory scale. The bedform three-dimensionality was imposed by shifting a standard two-dimensional (2D) dune in the streamwise direction according to a sine wave. Lefebvre (2014) also worked on flow separation and shear stress over the angle of repose bed-forms. They used the Delft3D modeling system to investigate the effects of bed form geometry and forcing conditions on flow separation length and associated turbulence, and bed form shear stress over angle-of-repose (30° lee side angle) bed forms. Lefebvre et al (2019) used a 3D numerical model that was set up with Delft3D and verified against lab experiments of idealized 3D bedforms. The model is used to simulate water velocities, turbulence, water levels, and bed shear stress above a natural bedform field from the Río Paraná (Argentina). In 2023, the researchers used RANS to simulate small-scale dunes and DES to simulate large-scale dunes. By employing these different turbulence models, they were able to account for variations in turbulence intensity and length scales that are important for accurately capturing the behavior of dunes at different sizes (Zhang et al. 2022). Geng et al. (2024) conducted a series of experiments on mobile bed dunes to accurately measure the morphology of two-dimensional and three-dimensional dunes under various flow conditions. This approach enabled them to examine the relationship between bed resistance and dune characteristics, including dune length, height, crest height, and trough depth, ultimately leading to the development of a new resistance relationship. The results revealed that bedload mass transfer within the riverbed plays a significant role in increasing bed resistance.

In their laboratory study, Cao et al. (2025) examined the load transfer of a mobile bed under various flow conditions and simulated the development of two- and three-dimensional dunes formed at different flow intensities. The results, which focused on bed morphology, revealed that the correlation coefficients of the longitudinal profile curve can be used as a quick and reliable indicator for distinguishing between two-dimensional and three-dimensional dunes. Van der Sande et al. (2025) developed a new morphodynamic model incorporating a hydrodynamic module solved in OpenFOAM, capable of capturing windbreak side effects such as flow separation. The model results indicated that, due to the increased surface roughness of the dune form, water depth rises by approximately 3–5% as the dune evolves from a flat bed. This evolution is accompanied by an increase in the effective roughness length of about 50–100%.

Typically, conducting experimental studies to assess the impact of bedforms on flow structure is both expensive and time-intensive. At the same time, numerical studies can enhance precision while decreasing both time and expenses. As mentioned in the previous section of the research history, the study of bed forms has predominantly focused on two-dimensional dunes, with only a few limited laboratory and field studies conducted on three-dimensional substrate dunes. Furthermore, in these studies, the hydraulic analysis of the flow structure has not been thoroughly and extensively examined, and most of the research has been approached from a morphological and descriptive standpoint. Additionally, the research conducted does not encompass a broad range of hydraulic conditions (e.g., Changes in bedform angle, crest height and curvature, and wavelength). As a result, this study was conducted to provide a more detailed investigation of the flow structure with changes in hydraulic parameters (bed angle, crest height, curvature, and wavelength), using numerical methods. In this study, the flow velocity field and shear stresses have been investigated and analyzed. It should be noted that the validation of the simulation results has been carried out with experimental results.

2. Materials and Methods

2.1. Basics of Theory

Governing equations

The equations that govern the modeling of a viscous incompressible fluid flow are the continuity equation and the Navier-Stokes equations, as presented below (Alfonsi 2009).

$$div(\bar{u}_i) = 0 \quad (1)$$

$$\rho\frac{\partial(\bar{u}_i)}{\partial t}+\rho\frac{\partial(\bar{u}_i\bar{u}_j)}{\partial x_j} = -\frac{\partial\bar{p}}{\partial x_i}+g.n + \frac{\partial}{\partial x_j}[\mu(\frac{\partial\bar{u}_i}{\partial x_j}+\frac{\partial\bar{u}_j}{\partial x_i})] + \frac{\partial}{\partial x_j}(-\rho\bar{u_i}^{'}\bar{u_j}^{'}) \quad (2)$$

The variables p and u represent velocity, x denotes location, t indicates time, i and j are Cartesian indices, P stands for pressure, and v refers to the kinematic viscosity of water.

The no-slip condition was applied to both the bed and side walls, while a layer of air with a height equal to twice the water depth was included in the computational domain to model free surface dynamics using the Volume of Fluid (VOF) method. Additionally, the VOF method was employed to calculate the free surface. The numerical solution approach utilized in this model is an implicit unsteady method. The VOF technique is suitable for scenarios involving two or more immiscible fluids and the interface between them. This method is based on the concept of fractional volume of fluid (VOF) and is demonstrated to be more flexible and efficient than other approaches for managing complex free boundary configurations. By solving these equations, the number α is obtained to indicate the volumetric ratio of the two fluid phases within each of the computational cells. For example, α = 1 indicates that the cell volume is full of water, α = 0 shows that the cell volume is full of air, and 0 < α < 1 is the transition zone between the two water and air fluids. For an incompressible fluid, the kinematic volume fraction is:

$$\frac{\partial F}{\partial t}+\frac{1}{V_F}\left[\frac{\partial(FA_iu_i)}{\partial x_i}\right] = \frac{1}{V_F}[\frac{\partial(\vartheta_F A_i\partial F/\partial_{X_i}}{\partial_{X_i}}] \quad (3)$$

Where, u_i = horizontal component of velocity; x_i = horizontal vector in the Cartesian coordinate system; VF = volume fraction of fluid in each cell; A_i = fractional areas open to flow in the i-coordinate of the Cartesian system; υ_F = diffusion coefficient and F = the volume of fluid per unit volume (Guide 2021).

$$\frac{\partial\alpha}{\partial t}+\nabla.(\alpha U)=0 \quad (4)$$

In the equation below density variation between two fluids has been shown:

$$\rho=\alpha\rho_w+(1-\alpha)\rho_a \quad (5)$$

The two-equation model (written in conservation form) is given by the following:

$$\frac{\partial(u_ik)}{\partial x_j}=P-\beta^*\rho\omega k+\frac{\partial}{\partial x_j}[(\mu+\sigma_k\frac{k}{\omega})\frac{\partial k}{\partial x_j}] \quad (6)$$

$$\frac{\partial(u_i\omega)}{\partial x_j}=\frac{\gamma\omega}{k}P-\beta\rho\omega^2+\frac{\partial}{\partial x_j}[(\mu+\sigma_\omega\frac{k}{\omega})\frac{\partial\omega}{\partial x_j}]+\frac{\rho\sigma_d}{\omega}\frac{\partial k}{\partial x_j}\frac{\partial\omega}{\partial x_j} \quad (7)$$

Where,

$P=\tau_{ij}\frac{\partial u_i}{\partial x_j}$ $\quad \tau_{ij}=\mu_t(2S_{ij}-\frac{2}{3}\frac{\partial u_k}{\partial x_k}\delta_{ij})-\frac{2}{3}\rho k\delta_{ij}$ $\quad S_{ij}=\frac{1}{2}(\frac{\partial u_i}{\partial x_j}+\frac{\partial u_j}{\partial x_i})$

And the turbulent eddy viscosity is computed from:

$\mu_t=\frac{\rho k}{\hat{\omega}}$ $\quad \hat{\omega}=\max[\omega, C\sqrt{\frac{2\bar{S}_{ij}\bar{S}_{ij}}{\beta^*}}_{\min}]$

$\bar{S}_{ij}=\frac{1}{2}(\frac{\partial u_i}{\partial x_j}+\frac{\partial u_j}{\partial x_i})-\frac{1}{3}\frac{\partial u_k}{\partial x_k}\delta_{ij}$

2.2. Modeling

2.2.1. Turbulence model

The Detached Eddy Simulation (DES) model, a hybrid approach combining RANS and LES, was initially proposed in Reference to lower the computational costs associated with the LES method (Spalart and Allmaras 1992). Over the past few decades, substantial progress has been made in integrating LES and RANS methods to develop a hybrid technique that leverages the strengths of both. DES is a single-equation hybrid model with two longitudinal scales, showing promising results, especially in cases of intense flow separation. In smooth boundary layer flows, RANS models offer the lowest computational cost while maintaining adequate accuracy, despite their limitations in handling intense flow separation. Conversely, the computational demands of LES in turbulent flows are high and are directly linked to the large Reynolds number. The current study utilized OpenFOAM software to analyze flow patterns in dunes. Known for its versatility in tackling various engineering tasks,

OpenFOAM stands out as an open-source tool. Unlike commercial computational fluid dynamics software such as Fluent and CFX, OpenFOAM requires defining project specifications for each sub-branch to create a model, followed by selecting a specific solver. In contrast, other software platforms only need input parameters to initiate problem modeling and solving. Selecting an appropriate solver poses a challenge when using OpenFOAM. In this study, the modeling employed version 9.0.1 of OpenFoam as the simulation solver, available on the Linux Ubuntu 21.0.4 operating system due to its open-source nature.

2.2.2. Boundary conditions

The fluid flow used in this simulation consists of water and air, and their thermophysical properties are presented in Table 1.

Table 1. Thermophysical properties of the used fluids in the simulation

Parameters	thermophysical properties
Density of water (kg/m^3)	1000
Air density (kg/m^3)	1.2
Kinematic viscosity of water (square meters per second)	10^{-6}
Kinematic air viscosity (square meters per second)	1.48×10^{-5}
Surface tension (N/m)	0.07
Gravitational acceleration (meters per second squared)	9.81

The model was set up with specified input and output boundary conditions. The "Velocity Inlet" was chosen for the input boundary condition, where the velocity is constant. On the other hand, for the output boundary condition, the "Pressure Outlet" was selected and equal to zero, which was also applied to the free water surface to account for atmospheric effects. The walls and bed of the channel were set using the "Wall", with equivalent roughness values of $1.5D_{50}$ and $2.5D_{84}$ for fine and coarse materials, respectively. More details are represented in Table 2. The water flow was assumed to be incompressible, with a density of 1000 kg/m³ and a dynamic viscosity of 0.001 kg/ms.

Table 2. Types of boundary conditions

Boundary	VOF	Pressure	Velocity
Inlet	alpha (water inlet height)	Zero Gradient	wave Velocity
Outlet	Zero Gradient	Atmospheric constant value	Zero Gradient
Bottom & Wall	Zero Gradient	Zero Gradient	No Slip
Atmosphere	Inlet Outlet	Total pressure	Inlet Outlet

2.2.3. Mesh generation

In general, selecting the optimal mesh size is considered one of the most crucial steps in numerical simulation. As the mesh becomes coarser, the gradients of variable changes may increase, leading to potentially inaccurate results (Wang et al. 2022). Therefore, a finer mesh should be used to allow for a more detailed examination of areas where flow variables experience sudden changes. This approach enables more accurate output by thoroughly analyzing all model variables within the computational domain. However, refining mesh sizes must be approached with caution, as it can increase the number of computational cells and extend computational time, which may not be cost-effective. Optimization should be conducted as a first step in numerical simulation. The effectiveness of Open-Foam's top solvers is influenced by the generated grid, as the grid's quality significantly impacts solution accuracy, computation time, and convergence. Thus, producing a high-quality grid is the initial crucial step in resolving any problem. In this work, the geometry was created in 3D using the OpenFOAM block-Mesh file. The specified dimensions were 0.6 meters in height, 0.9 meters in width, and 15.75 meters in length.

2.3. Experimental data

The laboratory model developed by Fazel Najafabadi (2018) was used to simulate the flow on dune bedforms (Fazel Najafabadi 2018). They conducted their experiments in a rectangular channel made of plexiglass with a length of 15.75 meters, a width of 90 cm, and a depth of 60 cm. The selected dunes have dimensions of 96 cm in length, 8 cm in height, and an angle of 8 degrees on the Lee side. Figure 1 shows a view of two types of three-dimensional dune bed forms made in the laboratory. According to the figure, two types of dunes have been used, including three-dimensional dunes with a convex crest line towards the downstream (Lobe) and three-dimensional dunes with a concave crest line towards the downstream (Saddle).

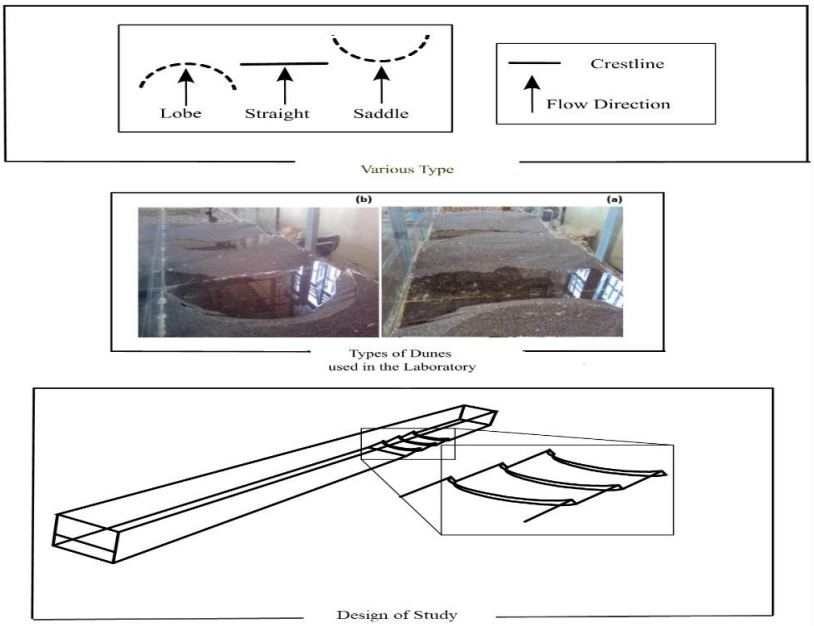

Figure 1. Structure of bedforms design (Fazel Najafabadi 2018)

The flow direction in all bedforms is from bottom to top. In this study, the flow structure on the dune bed was investigated using numerical simulations. Table 3 summarizes the hydraulic conditions used in the laboratory channel by Fazel Najafabadi (2018).

Table 3. Hydraulic conditions of experimental data (Fazel Najafabadi 2018)

Series	Dune Type	Flow Rate (lit/s)	Water Depth (cm)	Fr	$Re \times 10^5$
1	Lobe	30	26	0.15	0.22
2	Saddle	30	26	0.15	0.25

Table 4 displays particle size characteristics that were utilized in the laboratory.

Table 4. Geometric properties of sand particles (Fazel Najafabadi 2018)

Dune Type	d_{84} (mm)	d_{50} (mm)	d_{16} (mm)
Sand	13	10	6.73

2.4. Calibration

As mentioned earlier, to ensure the accuracy of the numerical results, the experimental results of Fazel Najafabadi (2018) were used to calibrate the numerical model. Furthermore, the validation results at 4 points on the dunes at two distances of 20 and 45 centimeters from the wall are presented. The position of the 4 points mentioned

for the bed form was as follows: on the stoss slope (p1), dune crest (p2), lee slope (p3), and the trough (p4). Figures 2 and 3 show the validation results of the dune bedforms. The top row of the figures illustrates the results at a distance of 20 cm from the wall, while the bottom row depicts the results along the central axis of the channel. The orange graphs are the profiles obtained from laboratory conditions, and the blue graphs are the simulated profiles. As shown in these figures, there is agreement between the experimental and simulated data.

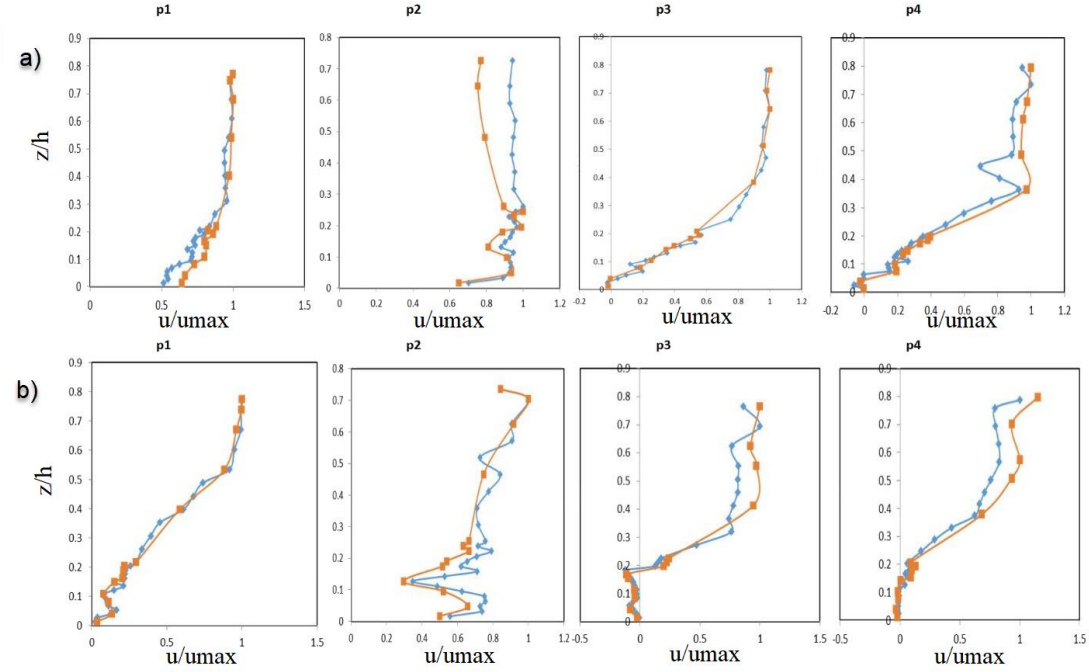

Figure 2. Comparison of velocity profiles in a dune (lobe) a) 20 cm from the wall b) 45 cm from the wall

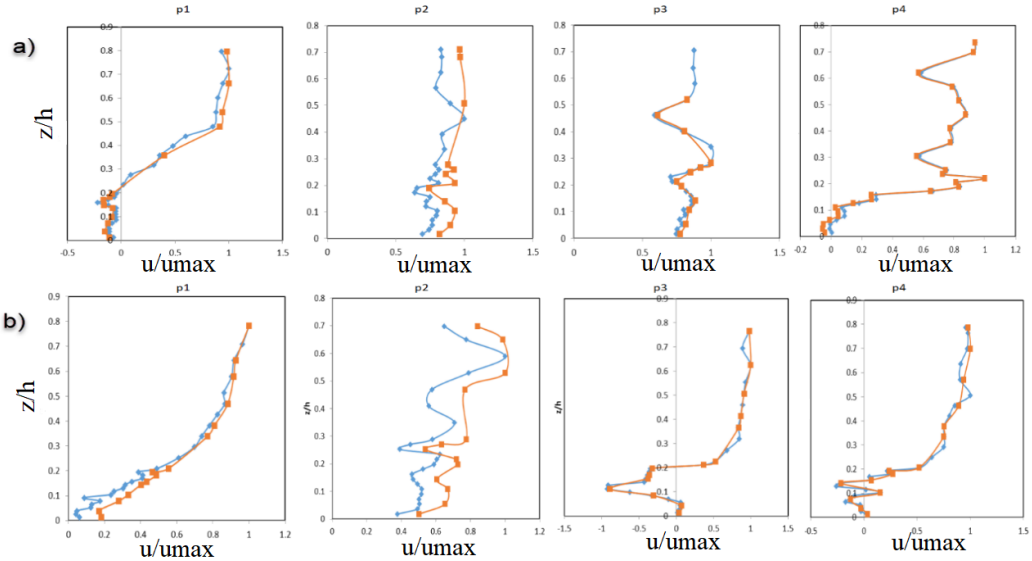

Figure 3. Comparison of velocity profiles in a dune (Saddle) a) 20 cm from the wall b) 45 cm from the wall

3. Results and Discussion

In this section, the velocity and shear stress contours are analyzed for two dune configurations: lobe and saddle. These contours are presented in two perspectives: a top view and a side view of the channel. The top view is illustrated on two planes with different z-

coordinates, while the side view is depicted at two distances of 20 cm and 45 cm from the wall.

3.1. Velocity profiles

Figure 4 displays four graphs depicting the contours of velocity with visibility from the side of the channel, x-z plane, at two distances: 20 cm from the wall (y=20 cm) and 45 cm from the channel wall (the central axis). The first column corresponds to the Lobe bed-form, while the second column corresponds to the Saddle bed-form.

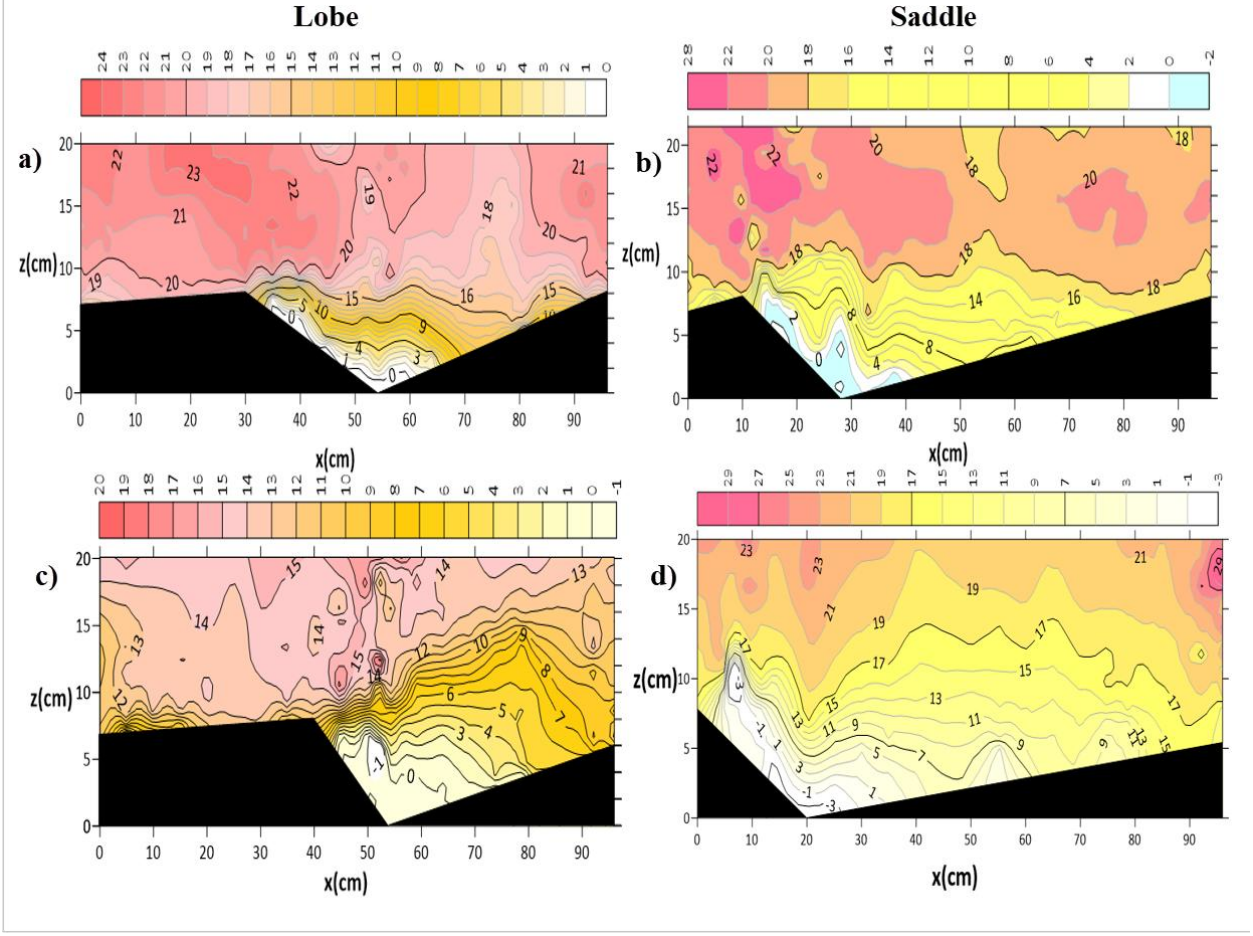

Figure 4. Stream-wise velocity contours, view from the side of the channel: a, b) Y=20cm; c, d) Y=45cm

As depicted in the figure, at a distance of 20 cm from the channel wall, the Lobe bed-form shows zero velocity or the beginning of the flow separation zone at x=53cm to x=60cm. The maximum velocity has also occurred near the water surface. In contrast, the Saddle bed-form exhibits a larger flow separation area and thus Stronger vortex flows, with negative velocities observed from x=10 cm to x=40 cm. This indicates that at 20 cm from the channel wall, both the length and depth of the flow separation zone in the Saddle bed-form are greater than those in the Lobe bed-form. Therefore, it can be stated that larger vortex flows have been created in the Saddle bed-form. It can also be noted that at 20 cm from the channel wall, the flow separation zone in the saddle bed-form exhibits larger values compared to the lobe bed. This observation is consistent with the central axis of the channel as well.

Diagrams (c) and (d) present the velocity contours along the central axis of the channel for the Lobe and Saddle bed-forms, respectively. In the Lobe dune, negative velocities are observed on the lee slope, indicating flow separation and vortex flow in this area (For the lobe, this area spans from x = 45 cm to x = 65 cm, and for the saddle, x=5cm to x=30cm). Conversely, in the Saddle bed-form, the negative velocities in the lee region are more pronounced, suggesting that both

the extent and length of the flow separation zone along the central axis of the channel are greater in the Saddle than in the Lobe. Additionally, it is important to note that in both graphs, there is an increase in velocity as the water level is approached. In a similar way, vortex flow has also been reported in the research of Omidyeganeh and Piomelli (2013) in the presence of three-dimensional dunes.

When comparing graphs a and c, which represent the distance of 20 cm from the wall and the central axis of the channel for the Lobe bed-form, it can be observed that as one moves from the channel wall toward the central axis, there is a decrease in velocity. Notably, the negative velocities are more pronounced on the lee side at the central axis, 20 cm from the channel wall. A similar trend is observed in the Saddle dune as well. This suggests that the flow diverges from the central axis toward the channel wall. The velocity gradients, or the density of the horizontal lines, are nearer to the bed at 20 cm from the channel wall, and they shift upward towards the water surface as they approach the central axis. Consequently, it can be asserted that the turbulence and flow intensity near the wall are closer to the bed, while along the channel's central axis, they exist at a higher elevation above the bed. This observation further corroborates the flow divergence.

Figure 5 shows the stream-wise velocity contours for both Lobe and Saddle dunes.

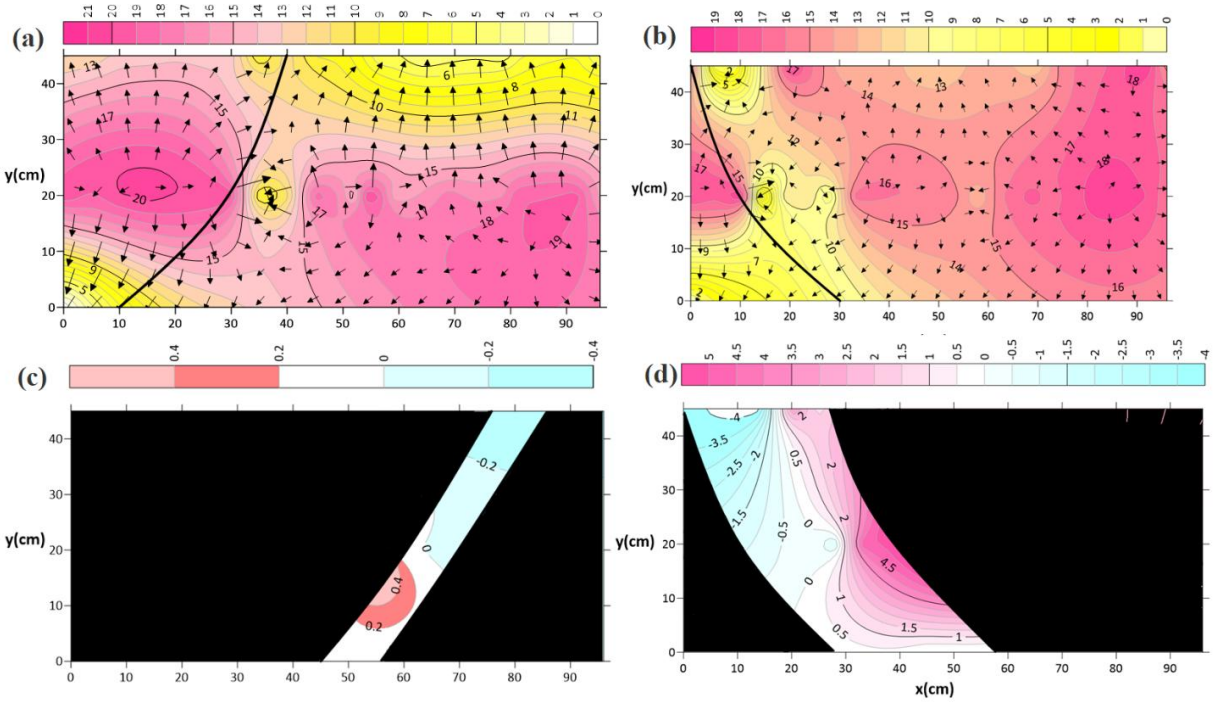

Figure 5. Stream-wise velocity contours, view from the top of the channel: a,b) z=83mm; c,d) z=21 and 33 mm

It is evident that the velocity gradients on the slope of Stoss and just before the crest line exceed those after crossing the crest line, which indicates a higher level of momentum and turbulence in that area. In this figure, x represents the flow direction, y indicates the transverse direction of the channel, and z denotes the height from the channel's bottom. As depicted, all four diagrams provide a top-down view of the channel, representing the x-y plane. Diagrams (a) and (b) display the velocity contours at the plane z=83mm, which is positioned 3mm above the crest line. Notably, all velocities at this plane are positive. The highest velocity in the lobe dune is observed near and just before the crest line, while in the saddle dune, the flow velocity increases progressively after the crest line, in the Saddle bed-form, on the stoss side, reaching its maximum at approximately x=85 cm. In both lobe and saddle dunes, the maximum velocity occurred at a distance of about 20 cm from the channel bank. Also, the velocity vectors in Figure

5a, b clearly show the formation of vortex flows immediately after the crest. These vortex flows affect the transverse and vertical velocity components and strengthen the secondary flows. Diagrams (c) and (d) present the velocity contours at z=21mm and z=33mm above the channel bottom, respectively. It's important to note that the black areas represent regions within the bed-form where there is no flow. Therefore, the flow velocity areas are located on the lee side. At this height above the bed, the maximum velocity was recorded at 15cm and 20 cm from the wall, respectively. As anticipated, due to its closeness to the bed, the value is less than at a height of 30 mm from the bottom of the channel. In both lobe-shaped and saddle-shaped, negative areas of velocity and flow separation are indicated, although this area is wider for the saddle. In both diagrams, it can be observed that at 20 cm from the channel wall, the negative velocities are lower compared to those at 45 cm from the wall. Additionally, these negative velocities are more pronounced along the central axis of the channel in the saddle region than in the lobe region. Or in other words, it can be said that by approaching the central axis of the channel, more flow separation has been observed. In addition, in areas where maximum velocity cores occur, the flow vectors show divergence. In contrast, flow convergence towards low velocity cores (the central axis of the channel) is observed.

3.2 Shear stress profiles

Next, it will be assessed and analyzed the results of the shear stress contours. Figure 6 illustrates the Reynolds shear stress contours from a side view of the channel, specifically along the x and z axes. Diagrams (a) and (b) present the Reynolds shear stress contours at 20 cm from the channel wall for the Lobe and Saddle bed-forms, respectively.

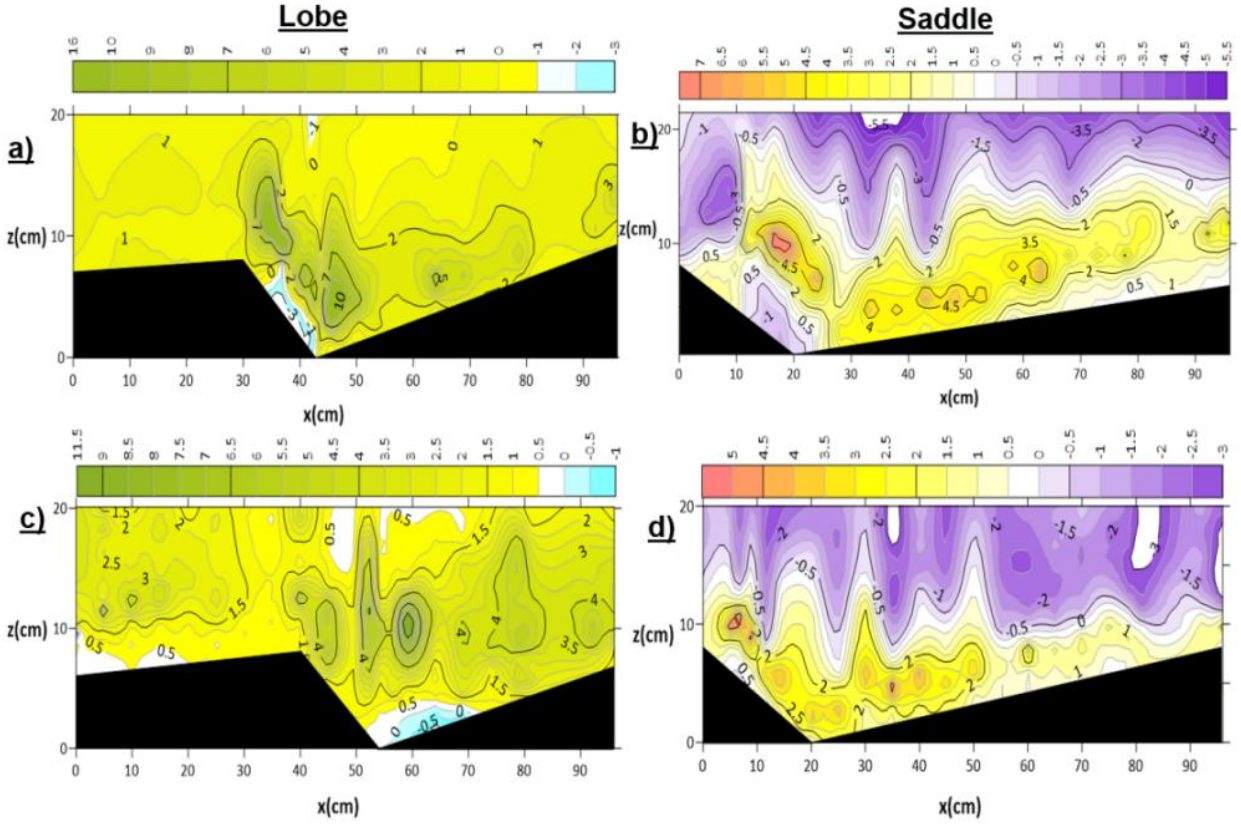

Figure 6. Reynolds shear stress contours, view from the side of the channel: a, b) Y=20cm; c, d) Y=45cm

The figure indicates that, in the Lobe bed-form, positive Reynolds shear stresses are observed, except in a portion of the lee slope area and a small region near the water surface. In

contrast, the Saddle bed-form displays significantly more negative Reynolds shear stresses, particularly near the water surface, highlighting that the Reynolds shear stresses exhibit nearly opposite behavior when transitioning from the Lobe to the Saddle bed-form.

In comparing graphs c and d, a similar pattern is observed at the central axis of the channel. In the Lobe bed-form, negative Reynolds shear stress is noted in a small area at the beginning of the stoss side, while in the Saddle bed-form, this Reynolds shear stress is positive. Additionally, unlike the Lobe bed-form, negative Reynolds shear stresses occur near the water surface in the Saddle bed-form.

When comparing diagrams (a) and (c), it is evident that at a distance of 20 cm from the wall, negative shear Reynolds shear stress is observed on the lee slope. In contrast, along the central axis, these negative shear Reynolds shear stresses appear at the beginning of the stoss slope. In the comparison of diagrams (b) and (d), it can be noted that at 20 cm from the wall, negative Reynolds shear stress occurs at the end of the lee slope. However, along the central axis of the channel, all Reynolds shear stresses on both the lee and stoss slopes are positive, with negative Reynolds shear stresses noted near the water surface. In summary, it can be stated that the reverse flows induced by pressure gradients are the cause of the change in the sign of the Reynolds shear stresses, as noted in the studies by Barbhuiya and Dey (Barbhuiya and Dey 2004; Dey and Barbhuiya 2006).

Figure 7 illustrates the contours of the Reynolds shear stress in the z=83 mm for the x-y plane, observed from above the channel, which is 3 mm above the crest of the dune.

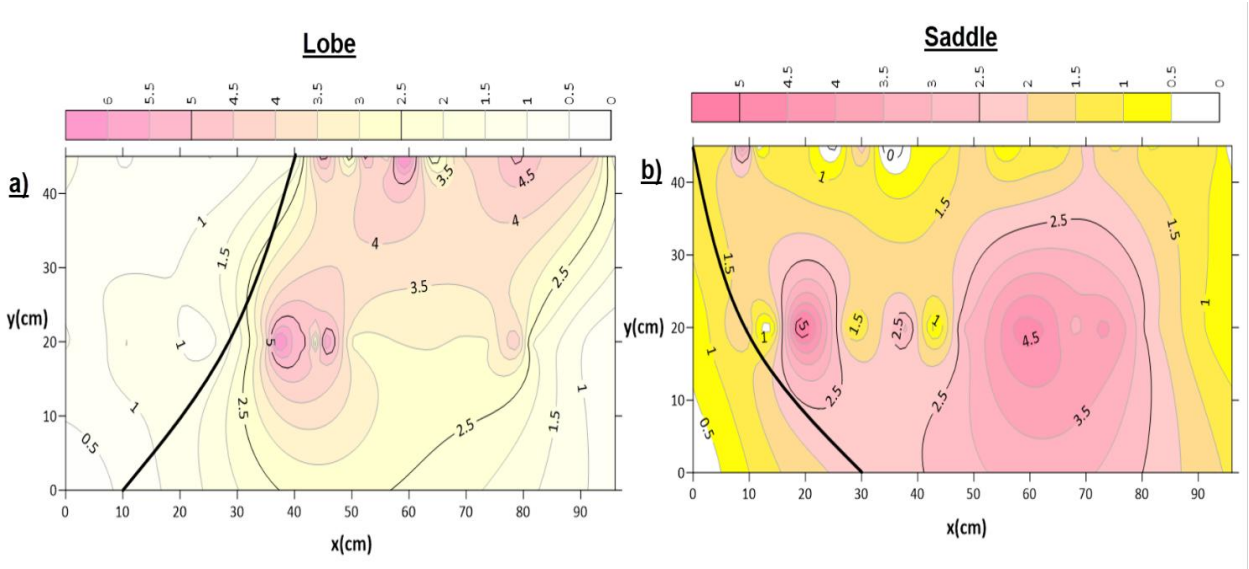

Figure 7. Reynolds Shear stress contours, view from the top of the channel: a) Lobe; b) Saddle

The figure shows that all the Reynolds shear stresses in this plane are positive. Comparing the two bed-forms, it is apparent that in both graphs, the maximum Reynolds shear stresses are equal and occur near the crest line at 20 cm, on the lee side. However, while the Lobe bed-form exhibits an increase in Reynolds shear stress as one moves toward the central axis, the Saddle bed-form shows a decrease in Reynolds shear stress. It can also be said that the region with the greatest shear stress effects resembles a pseudo-sinusoidal pattern, trending towards the central axis in the lobe dune, while in the saddle bed-form, it trends towards the channel wall.

3.3 Flow simulation with changing parameters

According to the goal of this research, in this section, the results of simulation by changing different parameters on the turbulent flow structure (velocity profiles and Reynolds shear stress profiles) on the dune bed-form (in two cases, lobe and saddle) have been considered.

3.3.1 Changing the lee side angle

a) Lobe

It has examined the variations in velocity and Reynolds shear stress profiles on the dune bed with a convex crest towards the downstream side (Lobe), while altering the exit angle (lee side angle) at three angles: 15, 28, and 32 degrees. It is important to note that as the angle changed, the wavelength remained constant, resulting in an inevitable increase in the height of the dune. These angles have been chosen based on prior research (MacVicar and Rennie 2012). Figure 8 shows velocity profiles, and Figure 9 shows Reynolds shear stress profiles. As mentioned in the Materials and Methods section, the four points examined in sequence are located at the stoss slope (p1), the dune crest (p2), the lee slope (p3), and the trough (p4).

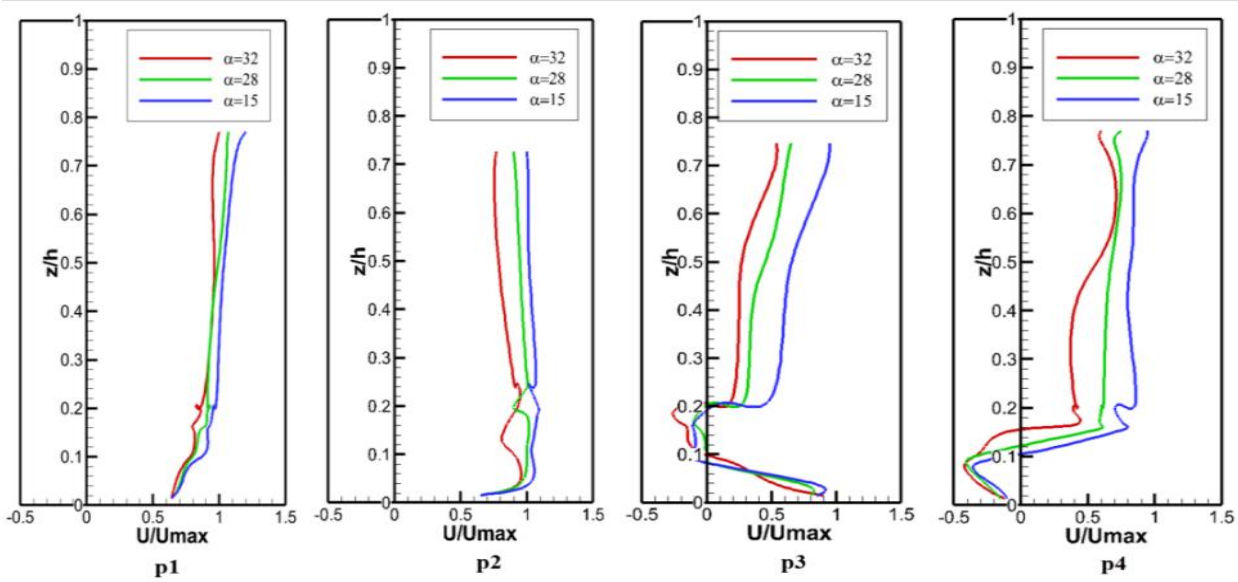

Figure 8. Comparison of the effect of the lee angle change on the velocity profiles on the Lobe

As depicted in Figure 8, the velocities on the stoss slope are consistently positive and exhibit a general pattern of increasing from the bed to the water level. At point p2, located on the dune crest, the velocity profiles show a rising trend from the bed to z/h=0.05. Subsequently, the profiles fluctuate until z/h=0.26, after which they gradually decrease towards the water level. On the lee slope or point p3, the velocity profiles are positive up to z/h=0.1, beyond which they maintain values up to z/h=0.2, indicating flow separation in this region. The figure illustrates that velocities at the 32-degree angle are lower than those at the other two angles. Beyond the flow separation zone, the velocities continue to be positive, displaying an increasing trend until the water level. In graph p4, the velocities for all three angles have been consistently decreasing from the start, with the minimum velocity occurring at z/h=0.8 for all angles (separation zone). Subsequently, for angles 15, 28, and 32, velocities reached zero at z/h=0.1, z/h=0.12, and z/h=0.16, respectively, and then increased to positive velocities until approaching the water surface.

In general, it is illustrated that by decreasing the lee angle, an increase in the velocity along the bed form (20% reduction at the dune crest, for the lobe- and saddle-shaped bedform, 50% and 10% reduction at the lee-side), and a decrease in the thickness of the flow separation occurred, which confirms the results presented by Motamedi et al. (2012).

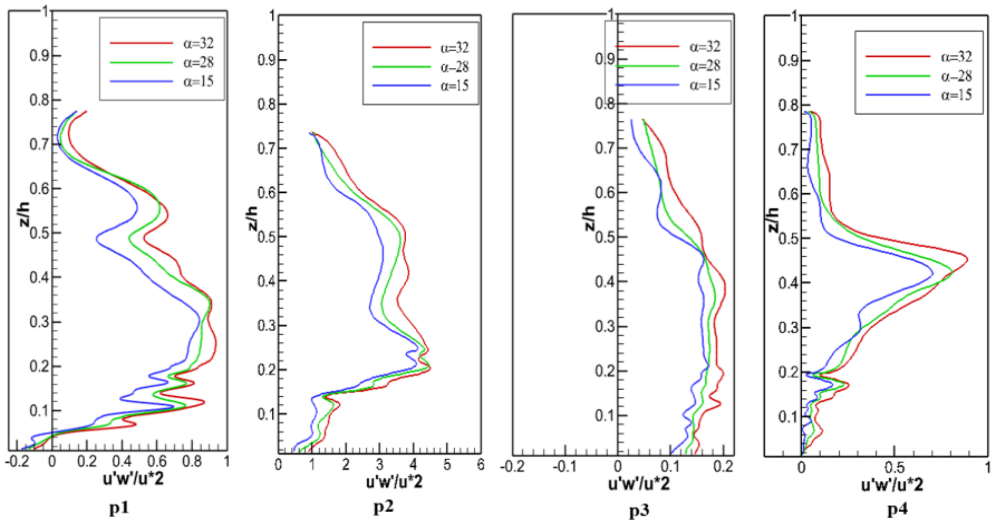

Figure 9. Comparison of the change in the lee angle on the Reynolds shear stress profiles on the Lobe

As shown in Figure 9, on the stoss side, shear stress took the negative values near the bed and then, by increasing the positive value, the maximum amount of shear stress occurred at z/h= 0.2. After that, Reynolds shear stress decreased up to the water surface. However, on the dune crest, the maximum Reynolds shear stress for all three angles was observed at z/h=0.2, with the highest Reynolds shear stress associated with the 32-degree angle. Beyond this point, the Reynolds shear stresses decreased until near the water level. Upon reaching the lee slope, the Reynolds shear stress profiles from the bed to the water surface exhibited positive values for all three angles. The Reynolds shear stress values for all three angles showed a very small gradient from the bed to z/h=0.46, and after this point, they displayed a decreasing trend toward the water surface with the higher gradient. Along the concave slope (Diagram P4), the Reynolds shear stresses from the bed for the three angles of 15, 28, and 32 degrees increased until z/h=0.42, z/h=0.4, and z/h=0.46, respectively, and then showed a decreasing trend until near the water level.

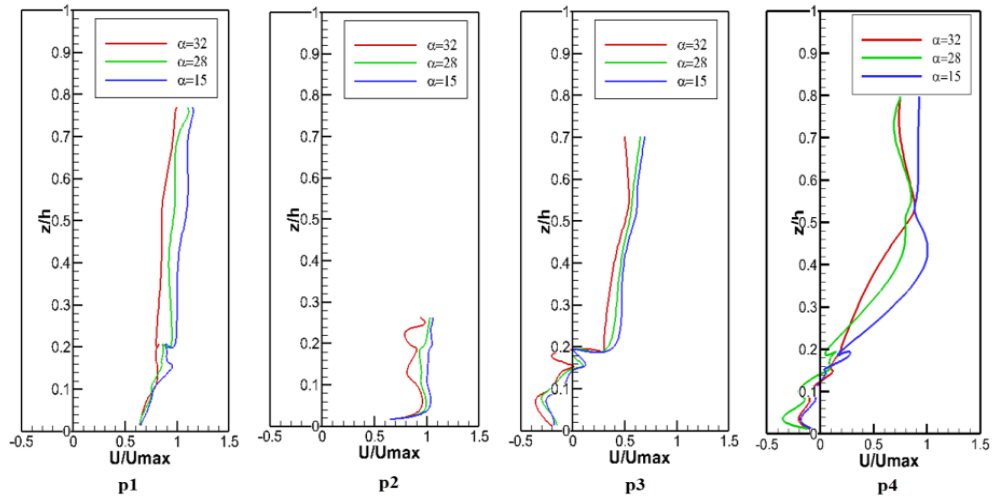

Figure 10. Comparison of the change in the lee angle on the velocity profiles on the saddle

The comparison of the profiles in different areas showed that as the flow progressed, the location of the maximum Reynolds shear stress moved towards the water surface, which is

consistent with the studies of Fazel Najafabadi (2018) and Motamedi et al. (2012). Overall, it can be observed that, like previous results, the lowest Reynolds shear stress occurred at a 15-degree angle.

b) Saddle

Figure 10 shows the results of the velocity profiles for the change of the outlet angle (lee angle) on four points of the saddle dune.

As shown in Figure 10, the velocity profiles on the stoss slope and on the crest of the dune, near the surface of the bed, respectively, up to z/h=0.1 and z/h=0.04, are almost coincident, and they did not have much difference with the change of angle. But from then until near the surface of the water, the highest velocity is related to an angle of 15 degrees. Entering the lee side and in the trough, it is illustrated that negative velocities are near the bed. These velocities are negative from the bed to the height of z/h=0.2 and z/h=0.14, respectively, which indicates the flow separation in these areas. In the p4 profile, the section exhibiting negative velocities showed a decrease with increasing angle; however, this trend was not observed in the section with positive velocities. As it is clear in the figure, the angle of 15 degrees has the lowest thickness of the flow separation zone near the bed. Next, Figure 11 illustrates the changes in Reynolds shear stress on the dune at 4 points of the bed-form.

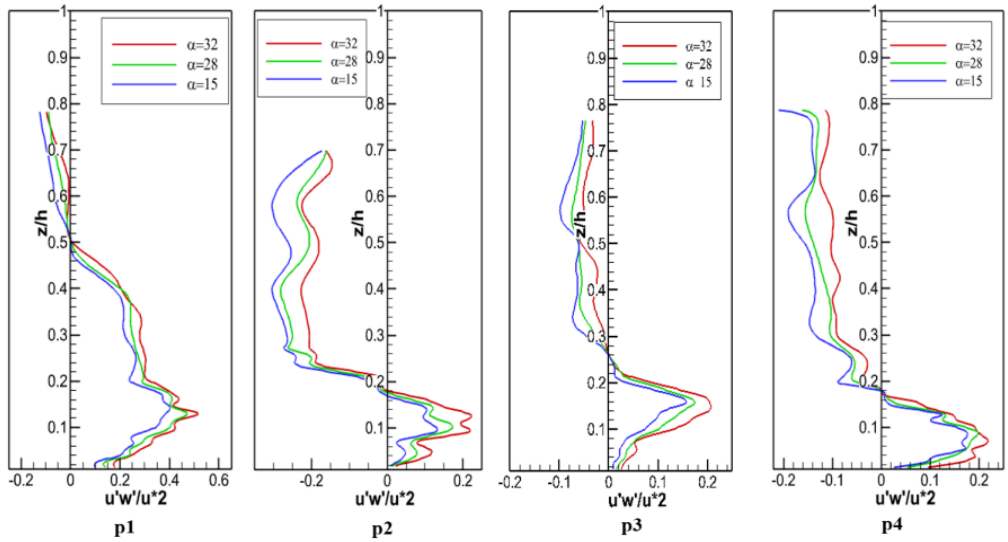

Figure 11. Comparison of the change in the lee angle on the Reynolds shear stress profiles on the saddle

According to Figure 11, the simulation results showed that on the stoss slope, Reynolds shear stresses with positive values increased from the bed up to z/h=0.13 and then decreased to zero until z/h=0.5. The decreasing trend continued after z/h=0.5, with the difference that the Reynolds shear stresses assumed negative values. In profiles p2, p3, and p4, as shown in the figure, it is evident that for all three angles, the shear stresses reach zero at z/h=0.18, z/h=0.26, and 0.18, respectively. After that, they decrease until reaching the water level. The profiles consistently showed that the highest Reynolds shear stress value occurred for the largest exit angle of the bed form (32 degrees). These findings align with the research conducted by Badzanchin et al. (2022).

As the comparisons indicated, previous studies have paid limited attention to changes in the slope of the downstream face. The present research demonstrated that increasing the slope, in both lobe and saddle configurations, can reduce the rate and extent of scour development.

3.3.2 Changing the wavelength of the dune bed-forms

a) Lobe

Figure 12 shows the changes in the velocity profiles for the changes of three different wavelengths (25, 70 & 96 cm). The selection of these parameters was made based on previous studies (Badzanchin et al. 2022, Motamedi et al. 2012). It is noteworthy that as the wavelength

changes, the input and output angles of the bedform remain constant; thus, the height of the bedform will inevitably vary. These profiles are drawn on the previously same 4 points on the dune bed-form.

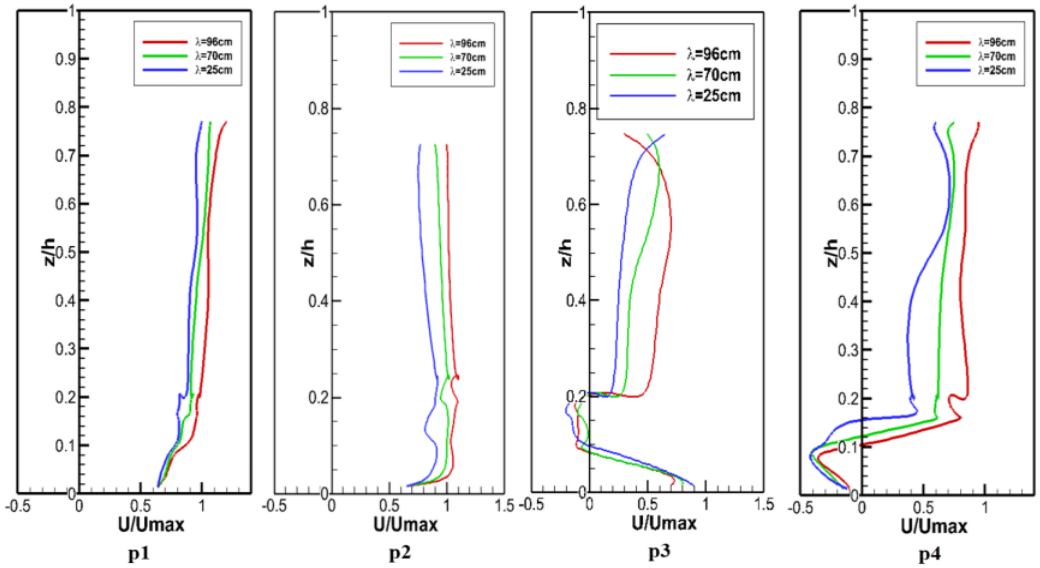

Figure 12. Comparison of wavelength change on velocity profiles on the lobe

As shown in Figure 12, the highest velocity from the bed to near the water surface on the stoss side and the crest of the dune was observed at the wavelength of 96 cm. It is indicated that flow separation has occurred in p3 and p4 profiles. At this point, it was also observed that the thickness of the flow separation zone was greater at a wavelength of 25 cm. After that, until near the water surface, the velocities increased with a small gradient, and the highest velocity occurred wavelength of 96 cm. In general, according to the graphs, it can be said that with the decrease in the wavelength of the bed form, a decrease in the velocities along the bed-form and an increase in the flow separation area on the lee side and through were observed. In general, the results showed that increasing the wavelength from 25 to 96 cm gave rise to a 20% stream-wise velocity reduction at the dune crest, for the lobe- and saddle-shaped bedform.

Figure 13 shows the changes in the Reynolds shear stress profiles for the changes in three different wavelengths.

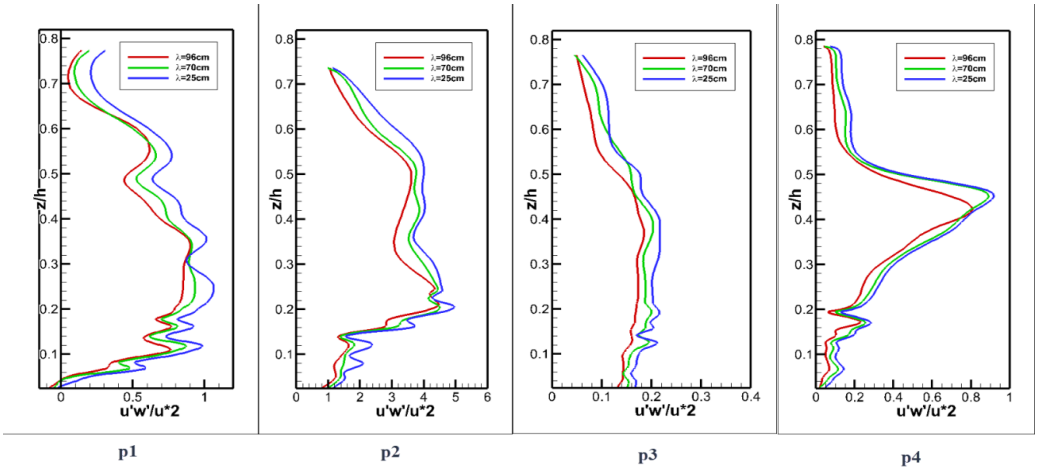

Figure 13. Comparison of wavelength change on Reynolds shear stress profiles on the lobe

In the figure above, the maximum stress for the profiles at points p1 and p2 was observed at z/h =0.26 and z/h = 0.2, respectively. p1 and p2 generally exhibited an upward trend. Subsequently, a decreasing trend was observed for all three wavelengths until the water level, with the highest Reynolds shear stress occurring at a wavelength of 25 cm. On the lee side, there is a lack of noticeable trend in Reynolds shear stress changes from the bed to z/h=0.44, with a very low gradient. After that, decreasing the Reynolds shear stress is shown up to the water surface. Additionally, in the trough line, the Reynolds shear stress profile from the bed showed an increasing trend for a wavelength of 96 cm until z/h=0.4, while the increasing Reynolds shear stress trend for wavelengths of 70 cm and 25 cm continued until z/h=0.46. Following this, the trend for all three wavelengths shifted to a decrease until near the water surface. Overall, it can be concluded that the highest Reynolds shear stress occurred at a shorter wavelength.

b) Saddle

Figures 14 and 15 depict the results of changes in velocity and Reynolds shear stress gradients with varying wavelength at 4 points on the saddle bed-form, respectively.

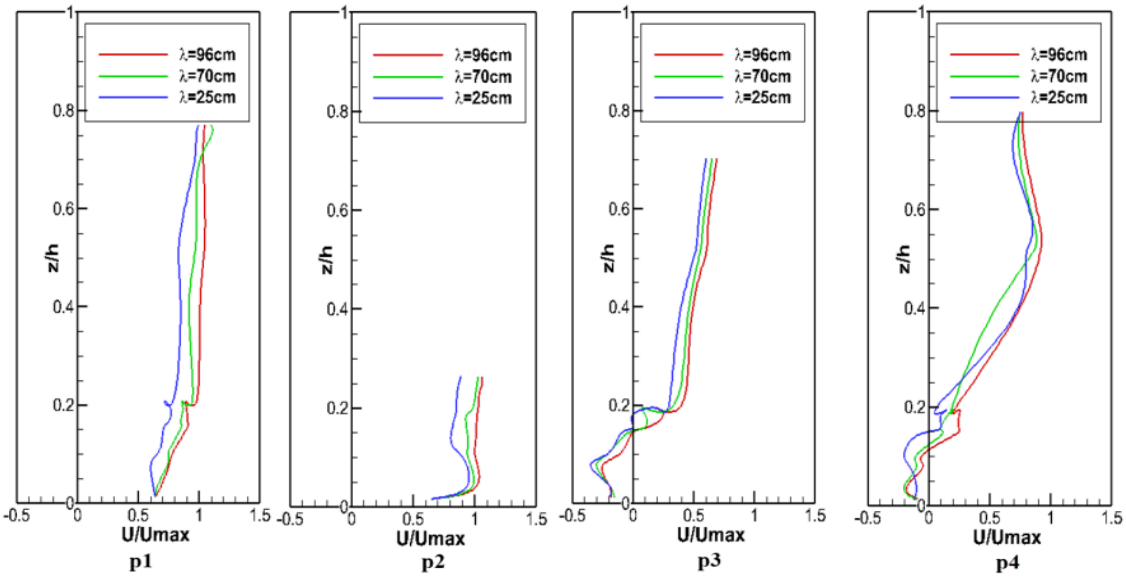

Figure 14. Comparison of wavelength change on velocity profiles on the saddle

As shown in Figure 14, the velocity gradients have exhibited an increasing trend on the stoss side from the bed to near the water surface; however, the gradients are lower near the water surface. Comparing the velocities for three different wavelengths showed that with a decrease in wavelength, the velocity decreased significantly, especially in the outer layer. On the lee side and at the trough line, negative velocities were observed near the bed, indicating flow separation in these areas. The thickness of the separated flow region for a 25 cm wavelength was greater compared to wavelengths of 70 and 96 cm. Upon passing through the separated flow region and the occurrence of positive velocities, the trend of increasing velocities continued up to the water surface. As observed, the velocity gradients decreased near the water surface. Overall, the highest velocities occurred for the largest wavelengths for all four profiles along the bedform. According to Figure 15 for all four selected profiles along the bedform, the increasing and decreasing trend occurred near the bed, and increasing the wavelength caused a decrease in the Reynolds shear stress generally. Then, on the stoss side and for a 25 cm wavelength, zero Reynolds shear stress was observed at z/h=0.7, while for the other two wavelengths, it was observed at z/h=0.5. On the crest of the bed-form, zero Reynolds shear stress occurred at approximately the same depth for all three wavelength values, at z/h=0.2.

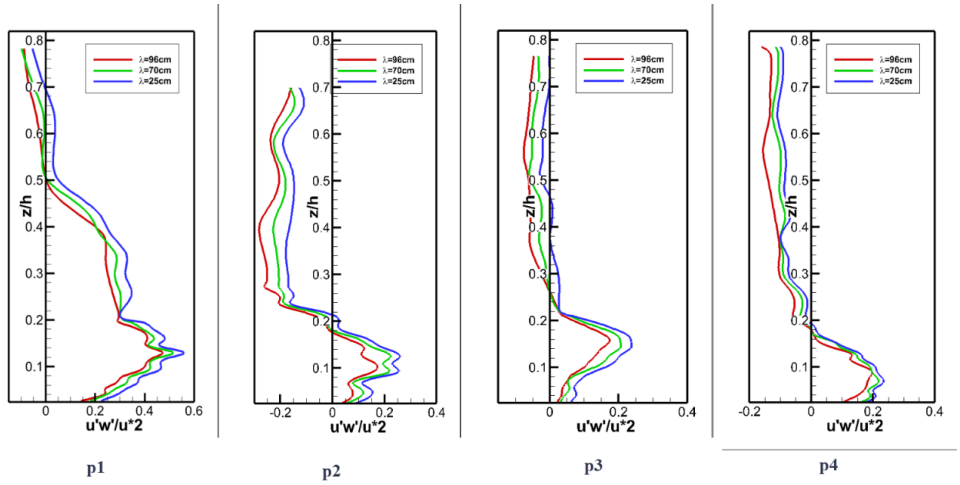

Figure 15. Comparison of wavelength change on Reynolds shear stress profiles on the saddle

On the lee side, for the 25 cm wavelength, zero Reynolds shear stress was observed at z/h=0.46, while for the 70 and 96 cm wavelengths, it was observed at z/h=0.26. Finally, at the last selected point on the trough line of the bed-form, zero Reynolds shear stress occurred at z/h=0.18. Further towards the water surface, it was observed that the occurrence of negative Reynolds shear stress values. As the results indicated, although an increase in wavelength reduced the shear stress between fluid layers, it simultaneously led to an increase in flow velocity. Therefore, selecting an appropriate wavelength and applying it in sandy rivers can play a crucial role in enhancing stream stability and supporting the development of aquatic habitats, which has rarely been considered in previous research.

3.3.3 Changing the curvature crest line of the dune bed-forms

Velocity and Reynolds shear stress profiles are examined in this section as the curvature of the dune crest line changes. Since previous researchers have not studied the impact of changing the crest line curvature parameter, the degree of crest line change was selected based on field observation. It is worth noting that in the experiments of Fazel Najafabadi (2018), a crest line curvature of 45 centimeters was used, modeled after the bedforms observed in sandy rivers. Considering this value as a baseline, two other values of 22.5 and 90 centimeters were chosen, which are respectively less and more than the amount used in the experiments. Therefore, three curvature crest line values of 22.5 cm (Low), 30 cm (Medium), and 90 cm (High) were investigated. This distance is the longitudinal distance from the curvature of the crest to the wall and the central axis. Figure 16 shows the results of the velocity profiles for changing the curvature crest line of the dune on four points of the dune bed-form with the convex crest line towards the flow downstream.

a) Lobe

In the Figure 16, the results of the simulations showed that on the slope of the stoss, the velocity values were very close to each other with changes in curvature, and significant variations were not observed; however, on the crest of the dune, a noticeable decrease (15% reduction) was observed with a reduction in the curvature of the crest line. All velocity profiles took a low gradient from near the bed to the water surface. Upon entering the lee side, the velocity gradient from the bed until z/h=0.1 was relatively high. After that, these values entered the negative region and caused the flow separation until z/h=0.2. From z/h=0.2, where the velocity was zero, to near the water surface, the velocity values were positive for three states, so that the lowest velocity occurred for the lowest curvature of the crest line; however, in the regions near the bed and the flow separation, the velocity values were very close to each other. The comparison of the thickness of flow separation also showed that the highest thickness occurred in the lowest curvature. At the trough of the dune, negative

velocities and a separation zone occurred near the bed, with the largest thickness of separation zone for the lower curvature. Then, positive velocities by taking an increasing trend were observed on the water surface. The higher velocities were demonstrated for the larger curvature.

Figure 17 shows the changes in the Reynolds shear stress profiles.

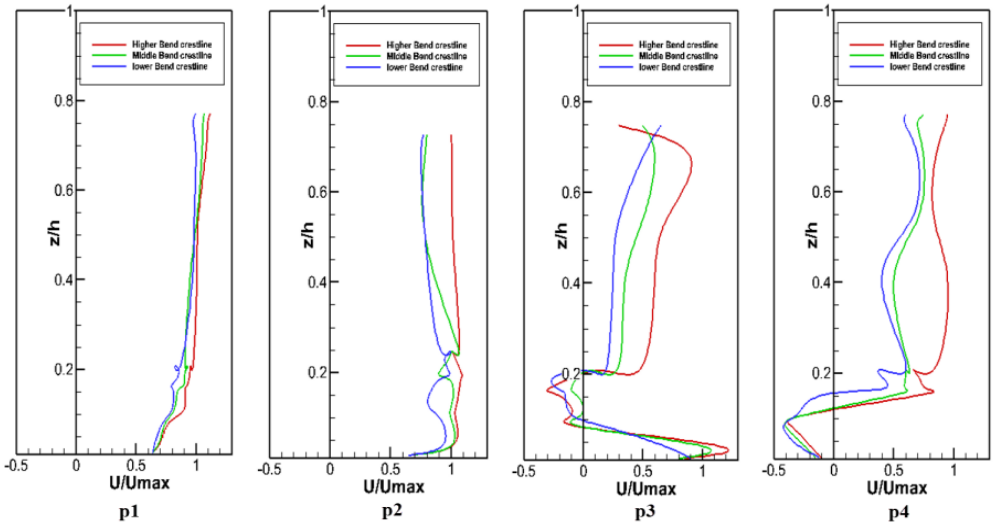

Figure 16. Comparison of the change in curvature crest line on velocity profiles on the Lobe

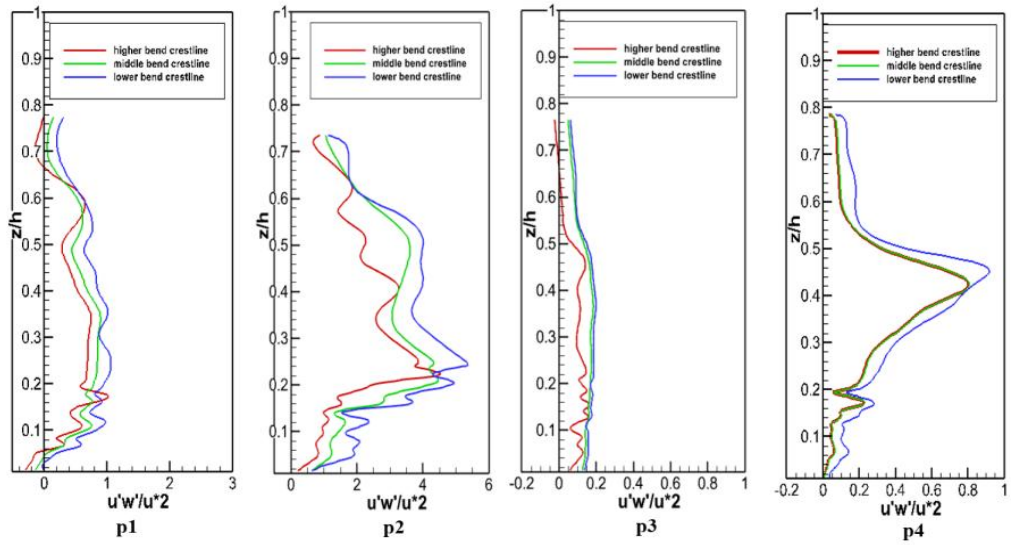

Figure 17. Comparison of the change in curvature crest line on Reynolds shear stress profiles on the Lobe

The simulation results showed that on the stoss side and on the dune crest, the Reynolds shear stresses with slight fluctuations increased up to z/h=0.18 and z/h=0.24, respectively, and then decreased up to the water surface. This occurred while, at both points, the highest Reynolds shear stress values occurred for the lowest crest curvature. Upon reaching the lee side and the trough line, the Reynolds shear stress gradients continued with very slight gradients from the bed to the water surface. However, the maximum Reynolds shear stress occurred at z/h=0.44 on the trough line. In general, it can be stated that with an increase in dune crest curvature in lobe mode, Reynolds shear stress decreases.

b) Saddle

First, the velocity profiles are examined, followed by the Reynolds shear stress at four points on the saddle-shaped bedform. (Figures 18 & 19).

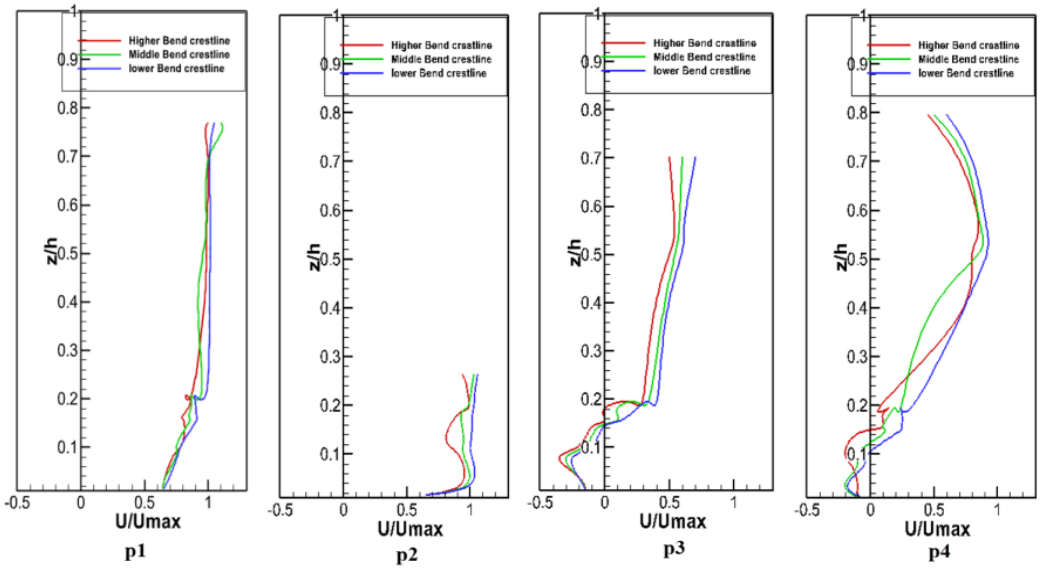

Figure 18. Comparison of the change in curvature crest line on velocity profiles on the saddle

As it is indicated in Figure 18, on the stoss side and the crest of the bed-form, the velocity profiles showed no significant changes with variations in the curvature of the crest, and had a small gradient from z/h=0.22 to the water surface. However, it can still be stated that the highest velocity occurred for the smallest curvature of the crest. Upon entering the lee side and at the trough line, as indicated in the figure, flow separation occurred near the bed up to z/h=0.16 and z/h=0.145, respectively, and the thickness of the separated flow region increased with increasing curvature of the crest. After that, the velocity values at both points became positive near the surface of the water, and the highest velocity corresponded to the smallest curvature of the crest (20% increase).

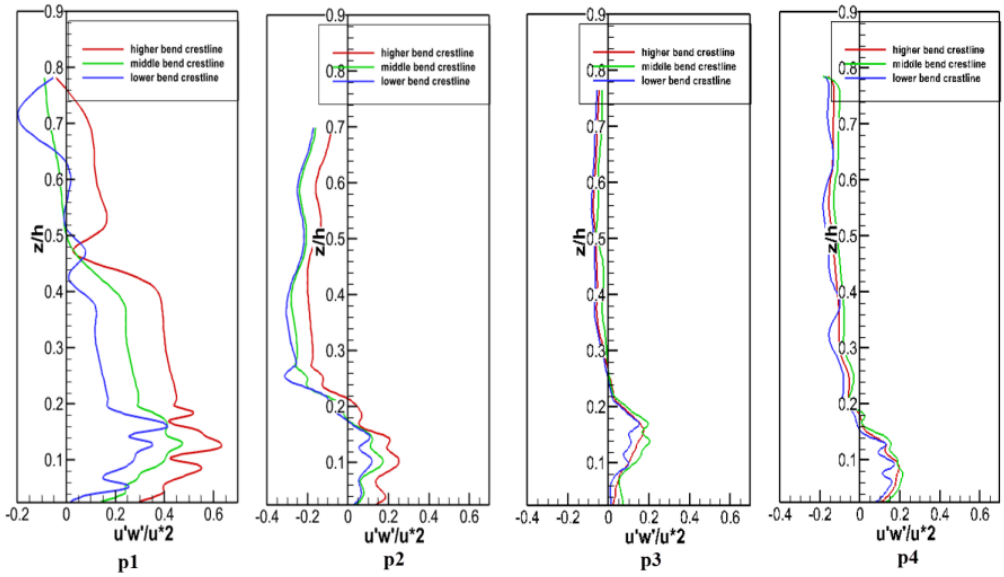

Figure 19. Comparison of the change in curvature crest line on Reynolds shear stress profiles on the saddle

The simulation results based on Figure 19 showed that Reynolds shear stresses on the stoss side, crest of the bedform, lee side, and trough line increased approximately up to z/h=0.18, z/h=0.1, z/h=0.18, and z/h=0.1. After that, a decrease in the water surface was observed. Reynolds shear stress has entered the negative phase for middle and lower curvatures at z/h=0.5 in P1. In the other three figures (p2, p3, and p4), the red, green, and blue curves have all entered the negative phase starting at approximately z/h = 0.2, z/h = 0.25, and z/h = 0.16, respectively. The negative Reynolds shear stress continued toward the water surface with a low gradient. In general, as can be inferred from the figure, it can be stated that with an increase in the curvature of the crest, the values of Reynolds shear stresses increased.

4. Conclusions

Results on the bedform with a convex crest downward (Lobe):

1. The results of changing the exit angle showed that with a decrease in the lee angle, an increase in velocity along the bedform and a decrease in the thickness of the separated flow were observed, while the results on the Reynolds shear stress showed that an increase in the angle led to an increase in Reynolds shear stress.

2. By reducing the wavelength of the bedform, a decrease in velocity along the bedform and an increase in the thickness of the separated flow on the lee slope and trough line were observed. Comparison of Reynolds shear stress components also showed that the maximum Reynolds shear stress occurred at a shorter wavelength.

3. By increasing the curvature of the crest, an increase in velocity and a decrease in Reynolds shear stress were observed.

Results on the bedform with a concave crest downward (Saddle):

1. With an increase in the lee angle, the velocity values decreased, and they also had the maximum flow separation thickness and stronger vortex flow near the bed on the lee slope and trough line. Meanwhile, the analysis of Reynolds shear stress components showed that with an increase in the angle, the Reynolds shear stress values also increased.

2. By changing the wavelength, the results showed that with an increase in the wavelength of the bedform, the velocity values also increased. However, the comparison of Reynolds shear stress showed that with an increase in the wavelength, the Reynolds shear stress along the bedform decreased.

3. By changing the curvature of the crest, a decrease in velocity and an increase in Reynolds shear stress for the highest curvature of the crest along the bedform were observed.

Among the existing limitations, the following points can be highlighted: The use of conventional turbulence models (such as k–ε or k–ω) provides only an approximation of the actual turbulent flow behavior and may not accurately capture the detailed three-dimensional eddy structures. Many input parameters—such as grain size, sediment density, bed roughness, and boundary conditions—carry inherent uncertainties that can influence the stability and accuracy of the results. To accurately reproduce 3D bedforms, a very fine computational grid is required; however, such long-term simulations with small time steps are highly time-consuming and computationally expensive. To advance the present research, it is recommended to develop coupled hydrodynamic–morphodynamic models to simulate flow and bed changes simultaneously. Employing more advanced turbulence models, such as LES or DES, is suggested to more accurately capture three-dimensional flow structures. Additionally, the use of adaptive mesh refinement (AMR) or data-driven approaches, including artificial intelligence, is advised to reduce computational costs and enhance prediction accuracy.

Author Contributions:

Masoumeh Ghodousi: Methodology, Formal analysis and investigation, Writing - original draft preparation, Resources.

Elham Fazel Najafabadi: Conceptualization, Writing - review and editing, Resources, Supervision.

Authors' Conflicts of Interest:

The authors declare no conflict of interest regarding the authorship or publication of this manuscript.

Data Availability Statement:

Data available on request from the authors.

References

Alfonsi, G. (2009). Reynolds-averaged Navier–Stokes equations for turbulence modeling. doi: 10.1115/1.3124648.

Ashley, G. M. (1990). Classification of large-scale subaqueous bedforms; a new look at an old problem. *Journal of Sedimentary Research*, *60*(1), 160-172. doi: 10.2110/jsr.60.160.

Badzanchin, M., Bahrami Yarahmadi, M., & Shafai Bajestan, M. (2022). Experimental Study of the Effect of the Dune Bed Form Height on Manning's Roughness Coefficient. *Irrigation and Drainage Structures Engineering Research*, *23*(87), 99-118. doi: 10.22092/idser.2022.359908.1522.

Balachandar, R., & Patel, V. C. (2008). Flow over a fixed rough dune. *Canadian Journal of Civil Engineering*, *35*(5), 511-520. doi: 10.1139/L08-004.

Best, J. (2005). The fluid dynamics of river dunes: A review and some future research directions. *Journal of Geophysical Research: Earth Surface*, *110*(F4). doi: 10.1029/2004JF000218.

Barbhuiya, A. K., & Dey, S. (2004). Measurement of turbulent flow field at a vertical semicircular cylinder attached to the sidewall of a rectangular channel. *Flow Measurement and Instrumentation*, *15*(2), 87-96. doi: 10.1016/j.flowmeasinst.2003.11.002.

Cao, W., Geng, X., Liu, C., & Zhang, L. (2025). Morphological properties of two-dimensional and three-dimensional bedforms in open channel flow: A flume experiments study. *International Journal of Sediment Research*, *40*(1), 15-30. doi: 10.1016/j.ijsrc.2024.09.007.

Cisneros, J., & Best, J. (2024). Controls on the leeside angle of dunes in shallow unidirectional flows. *Journal of Geophysical Research: Earth Surface*, *129*(3), e2023JF007520. doi: 10.1029/2023JF007520.

Dey, S., & Barbhuiya, A. K. (2006). Velocity and turbulence in a scour hole at a vertical-wall abutment. *Flow Measurement and Instrumentation*, *17*(1), 13-21. doi: 10.1016/j.flowmeasinst.2005.08.005.

Fazel Najafabadi, E. 2018. Effects of different 3D bed forms on coherent flow structure and boundary layer separation. Ph.D. thesis, Department of Agriculture, Isfahan University of Technology, Iran.

Geng, X., Cao, W., Liu, C., & Zhang, G. (2024). Experimental Study of Bedform Development Characteristics and Their Effects on Sediment Transport. *Applied Sciences*, *14*(21), 9823. doi: 10.3390/app14219823.

Gilbert, G. K. (1914). *The transportation of debris by running water* (No. 86). US Government Printing Office. https://books.google.com/books?hl=en&lr=&id=i3HVAAAAMAAJ&oi=fnd&pg=PA9&dq=Gilbert,+G.K.,+1914.+The+transportation+of+debris+by+running+water+(No.+86).

Grant, W. D., & Madsen, O. S. (1982). Movable bed roughness in unsteady oscillatory flow. *Journal of Geophysical Research: Oceans*, *87*(C1), 469-481. doi: 10.1029/JC087iC01p00469.

Guide G. S. 2021. Access mode: https://cfd. direct/openfoam/user-guide.

Hassanzadeh, Y., Abbaszadeh, H., Abedi, A., & Abraham, J. (2024). Numerical simulation of the effect of downstream material on scouring-sediment profile of combined spillway-gate. *AQUA—Water Infrastructure, Ecosystems and Society*, *73*(12), 2322-2343. doi: 10.2166/aqua.2024.360.

Lefebvre, A. (2019). Three-dimensional flow above river bedforms: Insights from numerical modeling of a natural dune field (Río Paraná, Argentina). *Journal of Geophysical Research: Earth Surface*, *124*(8), 2241-2264. doi: 10.1029/2018JF004928.

Lefebvre, A., Paarlberg, A. J., & Winter, C. (2014). Flow separation and shear stress over angle-of-repose bed forms: A numerical investigation. *Water Resources Research*, *50*(2), 986-1005. doi: 10.1002/2013WR014587.

Ma, F., Lü, P., Cao, M., Yu, J., & Xia, Z. (2024). Morphological and sedimentary characteristics of raked linear dunes in the southeastern Taklimakan Desert, China. *Aeolian Research*, *67*, 100923. doi: 10.1016/j.aeolia.2024.100923.

MacVicar, B.J. and Rennie, C.D., 2012. Flow and turbulence redistribution in a straight artificial

pool. *Water resources research*, *48*(2). doi: 10.1029/2010WR009374.

Maddux, T.B., Nelson, J.M. and McLean, S.R., 2003. Turbulent flow over three-dimensional dunes: 1. Free surface and flow response. *Journal of Geophysical Research: Earth Surface*, *108*(F1). doi: 10.1029/2003JF000017

Mazumder, B. S., Pal, D. K., Ghoshal, K., & Ojha, S. P. (2009). Turbulence statistics of flow over isolated scalene and isosceles triangular-shaped bedforms. *Journal of Hydraulic Research*, *47*(5), 626-637. doi: 10.3826/jhr.2009.3397

Motamedi, A., Afzalimehr, H., Singh, V. P., & Dufresne, L. (2014). Experimental study on the influence of dune dimensions on flow separation. *Journal of Hydrologic Engineering*, *19*(1), 78-86. doi: 10.1061/(ASCE)HE.1943-5584.000075.

Motamedi, A., Afzalimehr, H., Gallichand, J., & Abadi, E. F. N. (2012). Lee angle effects in near bed turbulence: An experimental study on low and sharp angle dunes. *International Journal of Hydraulic Engineering*, *1*(6), 68-74. doi:10.5923/j.ijhe.20120106.02

Ojha, S. P., & Mazumder, B. S. (2008). Turbulence characteristics of flow region over a series of 2-D dune shaped structures. *Advances in Water Resources*, *31*(3), 561-576. doi: 10.1016/j.advwatres.2007.12.001.

Omidyeganeh, M., & Piomelli, U. (2013). Large-eddy simulation of three-dimensional dunes in a steady, unidirectional flow. Part 2. Flow structures. *Journal of Fluid Mechanics*, *734*, 509-534. doi: 10.1017/jfm.2013.499.

Parsons, D.R., Best, J.L., Orfeo, O., Hardy, R.J., Kostaschuk, R. and Lane, S.N., 2005. Morphology and flow fields of three-dimensional dunes, Rio Paraná, Argentina: Results from simultaneous multibeam echo sounding and acoustic Doppler current profiling. *Journal of Geophysical Research: Earth Surface*, *110*(F4). doi: 10.1029/2004JF000231.

Raudkivi, A. J. (1963). Study of sediment ripple formation. *Journal of the Hydraulics Division*, *89*(6), 15-34. doi: 10.1061/JYCEAJ.0000952

Roushangar, K., Goodarzi, S., and Abbaszadeh, H. (2024). Numerical Investigation of the Performance of Blade Groynes on Scouring and its Effect on Hydraulic Parameters of Sediment and Flow. *Environment and Water Engineering, 10*(1), 121-136. doi: 10.22034/ewe.2023.388931.1851.

Sharifi, M., Tabatabai, M. R. M., & Najafabadi, S. H. G. (2023). Numerical simulation of flow structures over dunes to develop an empirical relationship for separation zone dimensions. *Flow Measurement and Instrumentation*, *89*, 102275. doi: 10.1016/j.flowmeasinst.2022.102275.

Spalart, P. and Allmaras, S., 1992, January. A one-equation turbulence model for aerodynamic flows. In *30th aerospace sciences meeting and exhibit* (p. 439). https://turbmodels.larc.nasa.gov/Papers/RechAerosp_1994_SpalartAllmaras.pdf.

Stoesser, T., Braun, C., Garcia-Villalba, M., & Rodi, W. (2008). Turbulence structures in flow over two-dimensional dunes. *Journal of Hydraulic Engineering*, *134*(1), 42-55. doi: 10.1061/(ASCE)0733-9429(2008)134:1(42).

van der Sande, W. M., Roos, P. C., Gerkema, T., & Hulscher, S. J. M. H. (2025). Nonlinear modeling of river dunes: Insights in long-term evolution of dune dimensions and form roughness. *Geomorphology*, *475*, 109649. doi: 10.1016/j.geomorph.2025.109649.

Van Rijn, L.C., 1993. *Principles of sediment transport in rivers, estuaries and coastal seas*. https://documentatiecentrum.watlab.be/imis.php?module=ref&refid=85377.

Venditti, J.G., 2003. *Initiation and development of sand dunes in river channels* (Doctoral dissertation, University of British Columbia). https://open.library.ubc.ca/media/download/pdf/831/1.0091228/2.

Wang, Z., Yang, J., Wang, W., Qu, J., Huang, X., & Zhao, W. (2022). Research on the flow-induced stress characteristics of head-cover bolts of a pump-turbine during turbine start-up. *Energies*, *15*(5), 1832. doi: 10.3390/en15051832.

Zhang, Y., Wang, P., & Shen, G. (2022). Characterizing and identifying bedforms in the wandering reach of the lower Yellow River. *International Journal of Sediment Research*, *37*(1), 110-121. doi: 10.1016/j.ijsrc.2021.08.003.